A Computationally-Efficient, Online-Learning Algorithm for Detecting High-Voltage Spindles in the Parkinsonian Rats

Ramesh Perumal, Vincent Vigneron, Chifen Chuang, Yen Chung Chang, Shihrung Yeh, Hsin Chen

A Computationally-Efficient, Online-Learning Algorithm for Detecting High-Voltage Spindles in the Parkinsonian Rats

Ramesh Perumal,[1] Vincent Vigneron,[2,3] Chi-Fen Chuang,[4]
Yen-Chung Chang,[4] Shih-Rung Yeh,[4] and Hsin Chen[1,5]

[1] Department of Electrical Engineering, National Tsing Hua University, No.101, Sec.2 Kuang-Fu Road, Hsinchu 30013, Taiwan, R.O.C.; [2]IBISC, EA 4526, Universite Evry, Universite Paris-Saclay, Saint-Aubin, France; [3]DSPCom, FAC/UNICAMP, Limeira, SP, Brazil; [4]Institute of Molecular Medicine, National Tsing Hua University, No.101, Sec.2 Kuang-Fu Road, Hsinchu 30013, Taiwan, R.O.C.; and [5]Biopro Scientific, Unit 312, Center of Innovative Incubator, No.101, Sec.2, Kuangfu Rd., *020)*

Abstract—Abnormally-synchronized, high-voltage spindles (HVSs) are associated with motor deficits in 6-hydroxydopamine-lesioned parkinsonian rats. The non-stationary, spike-and-wave HVSs (5-13 Hz) represent the cardinal parkinsonian state in the local field potentials (LFPs). Although deep brain stimulation (DBS) is an effective treatment for the Parkinson's disease, continuous stimulation results in cognitive and neuropsychiatric side effects. Therefore, an adaptive stimulator able to stimulate the brain only upon the occurrence of HVSs is demanded. This paper proposes an algorithm not only able to detect the HVSs with low latency but also friendly for hardware realization of an adaptive stimulator. The algorithm is based on autoregressive modeling at interval, whose parameters are learnt online by an adaptive Kalman filter. In the LFPs containing 1131 HVS episodes from different brain regions of four parkinsonian rats, the algorithm detects all HVSs with 100% sensitivity. The algorithm also achieves higher precision (96%) and lower latency (61 ms), while requiring less computation time than the continuous wavelet transform method. As the latency is much shorter than the mean duration of an HVS episode (4.3 s), the proposed algorithm is suitable for realization of a smart neuromodulator for mitigating HVSs effectively by closed-loop DBS.

Keywords—Parkinson's disease, Autoregressive modeling, Adaptive Kalman filter, Hilbert-Huang transform, Smart neuromodulator, Closed-loop deep brain stimulation.

Address correspondence to Hsin Chen, Department of Electrical Engineering, National Tsing Hua University, No.101, Sec.2 Kuang-Fu Road, Hsinchu 30013, Taiwan, R.O.C.. Electronic mail: hchen@ee.nthu.edu.tw

ABBREVIATIONS

AKF	Adaptive Kalman filter
AR	Autoregressive model
cDBS	Closed-loop deep brain stimulation
CWT	Continuous wavelet transform
DBS	Deep brain stimulation
FN	False negative
FP	False positive
FPGA	Field-programmable gate array
HHT	Hilbert-Huang transform
HVS	High-voltage spindle
LFP	Local field potential
ML	Machine-learning
PACF	Partial autocorrelation function
PD	Parkinson's disease
PSD	Power spectral density
SNR	Signal-to-noise ratio
TP	True positive
TR	Detection threshold
6-OHDA	6-Hydroxydopamine

INTRODUCTION

Parkinson's disease (PD) is the second most prevalent neurodegenerative disease, for which long-term medication usually becomes less or even adversely effective. Its major motor symptoms include resting

tremor, rigidity, bradykinesia, and postural instability.[15,21] Deep brain stimulation (DBS) has been a promising alternative for treating motor symptoms in advanced PD patients. It stimulates subthalamic nucleus, for example, with current pulses at a constant frequency (~ 130 Hz) to reset pathological neural synchrony, so as to alleviate the motor deficits in PD. However, such an "open-loop" DBS system stimulates the brain continuously at a constant frequency (~ 130 Hz), and is found to induce side effects such as distorted gait, impaired cognition or speech,[15] and shortens the battery life.[7] Therefore, stimulating the brain only upon the occurrence of pathological synchrony is desirable for minimizing the side effects and extending the battery life. This approach is called "closed-loop" DBS.

As PD mainly results from the depletion of dopaminergic neurons, the local field potentials (LFPs) recorded from the basal-ganglia-thalamocortical network are useful for indicating the state of a parkinsonian brain.[7,15,21,23] The elevated beta-band synchrony (15–30 Hz) in the LFPs is associated with bradykinesia and rigidity.[1,19,24,26] Several studies demonstrate that closed-loop DBS (cDBS) is superior to open-loop DBS in ameliorating the beta-band synchrony.[7,19,23,24,26] However, the resting tremor is not related to the beta-band synchrony,[1] but found more related to the abnormally-synchronized, high-voltage spindles (HVSs) in the basal-ganglia-thalamocortical network of 6-hydroxydopamine (6-OHDA) lesioned PD rats.[4,5]

HVSs are synchronous, spike-and-wave, rhythmic oscillations at 5-13 Hz.[12,13,31] In contrast to beta-band synchrony,[7,15,19,23,24,26] HVSs are relatively neglected in cDBS despite its prevalence in basal-ganglia-thalamocortical network after dopamine depletion.[4,5,12,13,31] An algorithm based on continuous wavelet transform (CWT) had been proposed for detecting HVSs of parkinsonian rats.[22] The simplified CWT algorithm was further realized in the field-programmable gate array (FPGA)[9] or a microcontroller[8] for closed-loop experiments. However, the HVS could only be detected after its onset for more than 500 ms in these cDBS systems, while the mean duration of an HVS episode is around 4.3 s (Table 1). The first 500 ms of HVS could already induce pathological changes in the basal-ganglia-thalamocortical network. Therefore, an algorithm able to detect the early-onset of HVS is demanded for minimizing the effects of HVSs.

Conventional machine-learning (ML) algorithms such as decision trees or neural networks are not considered in this study because HVSs vary widely across different brain regions and rats. These conventional algorithms need to be trained on all data from every brain region and rat. However, the non-stationary occurrence of HVSs usually results in insufficient

TABLE 1. The statistics of the training and testing datasets.

Dataset	Duration (min)	Total HVS Bursts	HVS density (Bursts/min)Mean ± Std	HVS duration (s)		HVS peak-to-peak amplitude (mV)		HVS distribution(%)		SNR (dB)	
				Range	Mean ± Std	Range	Mean ± Std	Range	Mean ± Std	Range	Mean ± Std
Training	20	142	6 ± 4	0.9–10.7	3.3 ± 1.6	0.5–4.6	1.2 ± 0.2	9–67	26 ± 10	2.8–15.1	9 ± 2.6
Testing	200	1131	5 ± 4	0.9–17.3	4.3 ± 2.4	0.3–4.8	1.3 ± 0.3	3–50	24 ± 9	3.3–15.3	9.2 ± 2.1

Refer to Supplementary S1 for the characteristics of each LFP recording in the training and testing datasets.

number of HVSs for training a conventional ML algorithm. Moreover, the ML algorithm contains a too large number of parameters, which not only increase model complexity but also become unfriendly for hardware implementation. Let N denotes the number of training examples, and d the data dimension. The training time complexity is $O(N.\log N.d)$ for decision trees, for example, and is $O(N(ij+jk+kl))$ for a 4-layer neural network with i, j, k, and l nodes in each layer.[10]

This paper proposes an unsupervised learning algorithm not only able to detect the early-onset of HVSs but also friendly for implementation in low-power, resource-constrained systems. The proposed algorithm is based on adaptive autoregressive modeling at interval,[3,11] and the model parameters are learnt online by an adaptive Kalman filter (AKF).[28] The main contribution of this article include (i) Developing an algorithm based on Hilbert-Huang transform to label 1273 HVS episodes. (ii) Identifying a low-dimensional, frequency-selective, autoregressive model for predicting HVSs from a very-short (6 samples, 144 ms) prior data. (iii) Developing the online-learning algorithm robust for adapting the model parameters to estimate the time-varying spectrum of HVSs even if LFPs are recorded from different brain regions or different rats. (iv) Evaluating the improved performance of the proposed algorithm in comparison with the CWT method over 1131 HVS episodes from four PD rats.

MATERIALS AND METHODS

Animals

Four male, 3–4 month-old Sprague-Dawley (BioLASCO Taiwan Co., Ltd., Taipei, Taiwan) rats (R_1-R_4) were kept under standard housing conditions at constant temperature (22 ± 1°C), humidity (relative, 50%), and 12-h light/dark cycles. Water was available *ad libitum*. Food intake was limited to 10-20 g/day to maintain constant animal weight. Animal care and surgery were approved by the Institutional Animal Care and Use Committee (Approval No.10321) of the National Tsing Hua University in Taiwan. All the experimental procedures in this study adhered to the animal guidelines regulated by the Council of Agriculture under the Animal Protection Act in Taiwan.

Stereotaxic Surgery

Rats were anesthetized for 1.5 h with Urethane dissolved in phosphate buffer solution (1.25 g/Kg) and 0.1 ml of Balanize, and then fixed in a stereotactic apparatus (Stoelting Co., IL, USA). 30 μg of 6-OHDA (6-hydroxydopamine hydrochloride; Sigma-Aldrich, St Louis, MO, USA) was dissolved in 6 μl of phosphate buffer solution containing 0.2% (w/v) ascorbic acid, and was then injected into the medial forebrain bundle (AP − 4.4 mm, ML +1.2 mm, DV − 8.8 mm from bregma) at a flow rate of 0.5 μl/min by using a dental needle (27G Terumo, Terumo Co., Tokyo, Japan). Four weeks following the injection of 6-OHDA, the lesioned group of rats were classified as successful PD models according to the amphetamine-induced rotational behaviour (Amp, 3 mg/kg, ip). The rotational speed of the PD rats was measured to be greater than six turns per minute. Stainless steel electrodes (0.002" in diameter, A-M Systems, USA) were implanted in the basal-ganglia-thalamocortical network for recording LFPs from layers 5b and 2/3 of the primary motor cortex, layers 5b and 2/3 of the secondary motor cortex, layers 5b and 2/3 of the primary somatosensory cortex, the dorsal region of striatum, and the ventrolateral thalamus.

Data Acquisition

The recording electrodes were connected to a headstage (T8G20, Triangle BioSystems, USA) with a voltage gain of 20. The LFPs were further amplified (x100) and band-pass filtered (0.1-1 kHz) by a differential amplifier (Model 1700, A-M Systems, USA). These recordings were digitized at a 1 kHz sampling rate and then saved on the computer by a PCI-6251 data acquisition card (National Instruments Corporation, Texas, USA). LFPs were recorded from eight brain regions of R_1 and from four brain regions of R_2-R_4 as the rats moved freely. R_1-R_4 were recorded for 47, 59, 60, and 20 minutes, respectively. The mean likelihood for HVSs to occur in these recordings was only 5.9%. Therefore, out of each recording channel was an 11-minute-long LFP extracted (Supplementary S1) to contain not only all HVSs but also non-spindling segments before and after the occurrence of HVSs. Non-spindling segments are still more than HVS segments to mimic the real situation, as well as to evaluate the algorithm's robustness against different background noises.

Each extracted LFP was further divided into one-minute-long training data plus 10-minute-long testing data. The training dataset is used to identify the optimal model order and interval (p^* and τ in Section Autoregressive Modeling), the learning rate (Supplementary S4), and detection thresholds (Supplementary S7) for the proposed algorithm, while the testing dataset is used to examine the algorithm's ability to adapt model parameters ($\boldsymbol{w}_n$ in Eq. (2)) by online learning. The performance of the proposed algorithm is further compared with the CWT algorithm through computer simulation (Section Perfor-

mance Comparison) with MATLAB R2020a (The Mathworks, Natick, MA, USA). Moreover, the training and the testing datasets exhibit similar mean HVS distributions and signal-to-noise ratios (SNRs) across the four rats. Table 1 summarizes the statistics on the density, duration, peak-to-peak amplitude, distribution, and SNR of HVSs in the datasets. Obviously, the HVS is a non-stationary signal with great variability, making it difficult to detect HVSs reliably with a simple threshold.

Labeling HVSs by Hilbert-Huang Transform

The onset and end of HVS episodes are detected by the spike-and-wave pattern and the oscillation frequency (5–13 Hz).[12] The Hilbert-Huang transform (HHT) has been used to analyze non-stationary signals with the data-driven basis functions to achieve sharp time and frequency localization.[18] The raw LFPs from the primary motor cortex (layer 5b) of R_2 in Fig. 1a show the spike-and-wave pattern of HVSs (t_1–t_2, t_3–t_4). LFPs are analyzed with HHT to compute the instantaneous frequency and energy. The Hilbert spectrum (Fig. 1b) is obtained by plotting the energy in the time-frequency plane to show the time-varying spectra of HVSs. The mean HVS energy (Fig. 1c) is determined by averaging the energies over the 5-13 Hz band. It is further smoothed by the Gaussian window of length 200 ms.

HVSs exhibit higher energy (Fig. 1b) between 5 and 13 Hz resulting in higher mean HVS energy (Fig. 1c) than the non-spindling LFPs. The HVS onset (t_1 or t_3 in Fig. 1) is defined as the timestamp at which the mean HVS energy exceeds a predefined threshold (TR) for 200 ms. Over-threshold timestamps that do not show the spike-and-wave pattern are rejected. TR is computed by Eq. (1) using the mean μ and standard deviation σ of the mean HVS energies over the 1-s-long non-spindling LFPs.

$$TR = \mu + \beta\sigma \tag{1}$$

The scaling factor β and TR are identified for each LFP recording in the training dataset (Supplementary S2). This algorithm is used as the gold standard method to label HVSs in this study.

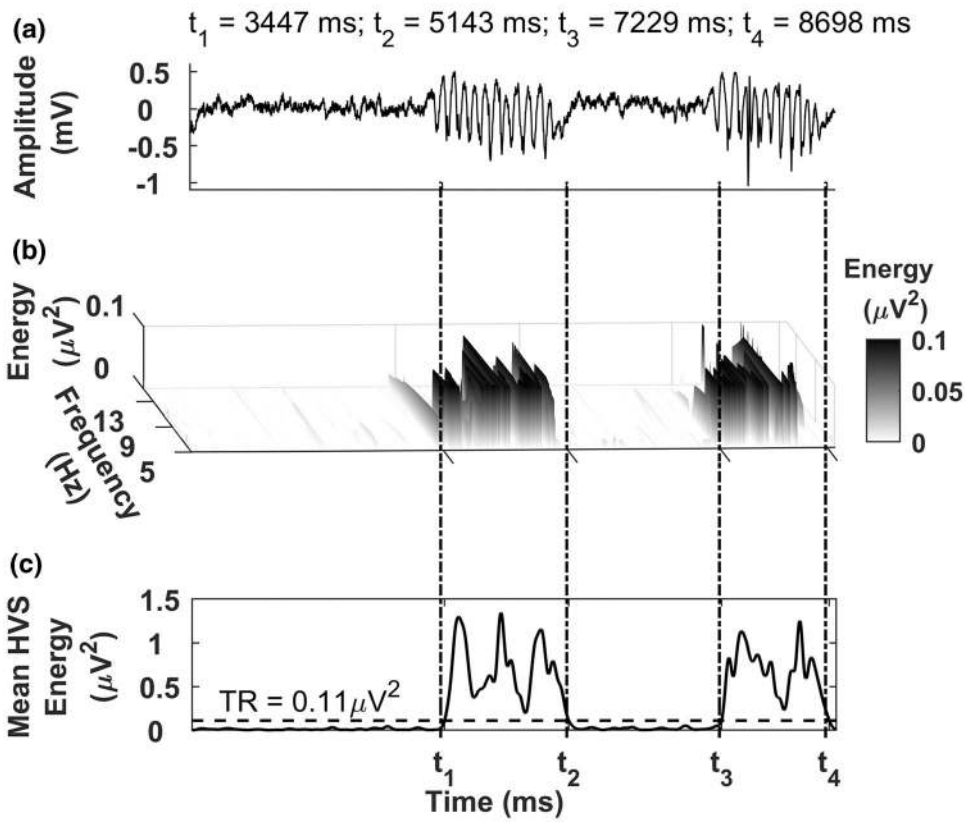

FIGURE 1. (a) LFPs recorded from the primary motor cortex (layer 5b) of R_2; (b) Corresponding Hilbert spectrum computed by HHT. Colors are scaled from minimum (white) to maximum (black) values of energy. (c) Temporal distribution of mean HVS energy showing the increase in energy during the occurrence of HVSs.

Autoregressive Modeling

Eight one-minute-long LFPs in the training dataset were band-pass filtered to extract the HVSs in the 5-13 Hz band. The autocorrelation functions[2] of the filtered LFPs are shown in Fig. 2a. The exponentially-decaying, sinusoidal oscillations in Fig. 2a imply that the transient dynamics of HVSs are underlain by a high-order autoregressive (AR) model.[2] Let $\mathrm{AR}_\tau(p^*)$ denotes the AR model with a model order p^* and a sampling time-lag τ, and $\mathrm{AR}_1(p)$ the p-order standard AR model with $\tau = 1$. For ease of reading, $\mathrm{AR}_1(p)$ is replaced by $\mathrm{AR}(p)$ in the following. For a time series $(x_1, x_2, \ldots, x_N)^T$ of length N, the value x_n at discrete-time n could be predicted by the $\mathrm{AR}_\tau(p^*)$ model as $\hat{x}_n$ from the past p^* observations according to Eq. (2):

$$\begin{aligned}\hat{x}_n &= \sum_{i=1}^{p^*} x_{n-i\tau} w_i(n) + r_n \\ &= \boldsymbol{x}_{n-\tau}^T \boldsymbol{w}_n + r_n\end{aligned} \tag{2}$$

where $\boldsymbol{x}_{n-\tau} = \left(x_{n-\tau}, x_{n-2\tau}, \ldots, x_{n-p^*\tau}\right)^T$ consists of past p^* samples, equally-separated by the time interval of τ. $\boldsymbol{w}_n = \left(w_1(n), w_2(n), \ldots, w_{p^*}(n)\right)^T$ is the coefficient vector. r_n is a zero-mean, white Gaussian noise with variance σ_R^2. Predicting $\hat{x}_n$ with the standard $\mathrm{AR}(p)$ model consists simply in substituting p for p^* and setting $\tau = 1$ in Eq. (2).

The selection of p and p^* depends ultimately on the feature of interest and the resulting performance. The first peaks in Fig. 2a indicate the LFPs exhibit a higher degree of linear predictability at the time lag of 143 ms. Therefore, setting $p = 143$ could enhance the predictability of HVSs for the standard $\mathrm{AR}(p)$ model.[14] However, the standard $\mathrm{AR}(p)$ model could often lead to over-smoothed temporal and spectral estimates for frequency-selective oscillations.[3,11] A high-dimensional model also demands more computing resources in hardware implementation. To discriminate the distinct spectral peaks of spindling and non-spindling LFPs accurately, as well as to make the algorithm hardware-friendly, the $\mathrm{AR}_\tau(p^*)$ model is preferable.[3,11]

The optimal model order p^* is identified by calculating the partial autocorrelation functions[2] (PACFs) of the eight filtered LFPs in the training dataset. The PACF includes only the direct correlation between the time series and its value at time lag δ, and the PACF of an ideal $\mathrm{AR}_\tau(p^*)$ process approaches zero as δ increases beyond the optimal p^*. As shown by Fig. 2b, the PACFs are very close to the 95% confidence interval when δ increases beyond 6. Therefore, the optimal p^* is chosen as 6 and τ as 24, such that the effective model order of $\mathrm{AR}_\tau(p^*)$ $(= p^* \times \tau = 144)$ approximately equals p. The model parameters are further cross-validated on the other 12 LFPs in the training dataset to evaluate the goodness-of-fit metrics (defined in Appendix A).

The On-Line Learning Algorithm

The Kalman filter is widely used in closed-loop algorithms to estimate the control signals with less computational load.[27,29] The standard $\mathrm{AR}(p)$ model had been employed to describe the temporally-evolving harmonics in the LFPs.[16,20] According to the analysis in Section Autoregressive Modeling, this study employs the $\mathrm{AR}_\tau(p^*)$ model instead to predict the onset of HVSs. The model coefficients are learnt online by AKF[28] using the architecture in Fig. 3b. Each raw LFP $\boldsymbol{d}(n)$ first undergoes the preprocessing steps in Fig. 3a (detailed in Supplementary S3) to obtain $\boldsymbol{x}(n)$ to facilitate faster convergence of $\boldsymbol{w}_n$. $\boldsymbol{x}(n)$ is di-

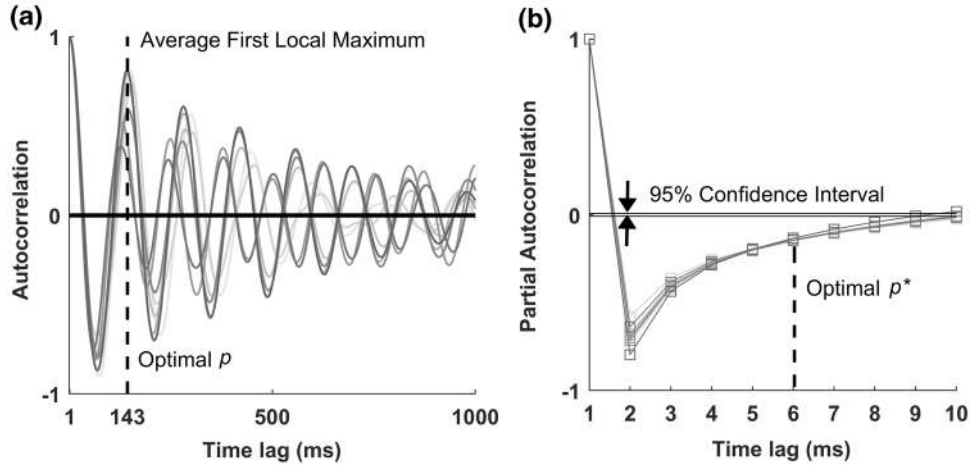

FIGURE 2. (a) Autocorrelation functions and (b) Partial autocorrelation functions of eight band-pass filtered LFPs in the training dataset.

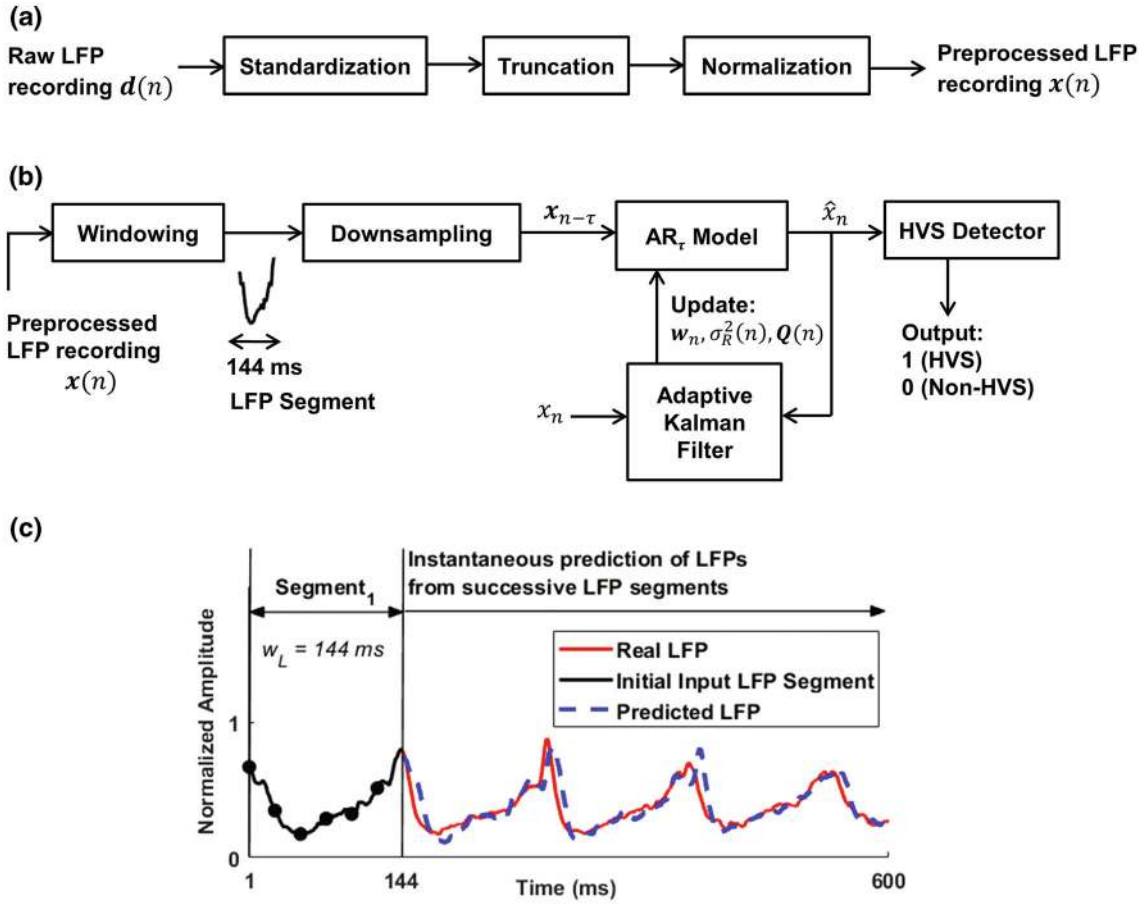

FIGURE 3. (a) Preprocessing steps for raw data; (b) The prediction and detection architectures in the online-learning algorithm; (c) The timing relationship among the observed LFP, the prediction input, and the LFP predicted by the online-learning AR$_\tau$ model.

vided into segments (e.g. Segment$_1$ in Fig. 3c) by overlapping sliding windows of length w_L = 144 ms, and then downsampled by a factor of τ as $\boldsymbol{x}_{n-\tau}$ (the black dots in Fig. 3c). Two successive LFP segments are separated by the time interval d_L = 1 ms. In other words, the algorithm predicts the onset of HVS every 1 ms.

Given an initial LFP segment of 144 ms (the black curve in Fig. 3c), the AR$_\tau$ model estimates $\hat{x}_n$ for every time step (the dashed blue curve in Fig. 3c). According to the difference between the real x_n (the red curve in Fig. 3c) and the estimated $\hat{x}_n$ at each time step, the AKF not only updates $\boldsymbol{w}_n$ but also tunes the measurement noise variance $\sigma_R^2(n)$ and the process noise covariance matrix $\boldsymbol{Q}(n)$ (see Appendix B for detailed formula). The HVS detector estimates the power spectral density (PSD) from $\boldsymbol{w}_n$ to determine the HVS power P_{AKF} (Appendix B). The LFP segment is classified as HVS if P_{AKF} exceeds a predefined threshold.

Performance Evaluation

Detection of HVSs by Continuous Wavelet Transform

LFPs are analyzed in MATLAB by CWT with the complex Morlet wavelet.[22] The wavelet energy $\boldsymbol{E}(t,f)$ over time t and frequency f is computed as the square of CWT coefficients $\boldsymbol{C}(t,f)$ as:

$$\boldsymbol{E}(t,f) = |\boldsymbol{C}(t,f)|^2; \boldsymbol{e}(t) = \int_5^{13} \boldsymbol{E}(t,f)df \qquad (3)$$

The HVS energy $\boldsymbol{e}(t)$ in Eq. (3) is computed by summing $\boldsymbol{E}(t,f)$ over the bandwidth of 5-13 Hz. The time-frequency distribution of $\boldsymbol{E}(t,f)$ (Supplementary S6) is used to characterize the spectrotemporal features of HVSs.[22] In the CWT-based detection algorithm, the raw LFPs are segmented by windowing with w_L = 512 ms and d_L = 24 ms. The value of w_L should be greater than 500 ms to achieve the time-frequency resolution required for reliable detection of HVSs. The value of d_L is chosen in accordance with the value of τ in the AR$_\tau$ model, so as to reduce computational load without degrading detection perfor-

mance. As shown in Eq. (4), the HVS power P_{CWT} is determined by averaging $\boldsymbol{e}(t)$ over the duration w_L of each LFP segment.

$$P_{CWT} = \frac{1}{w_L} \int_0^{w_L} \boldsymbol{e}(t)dt \tag{4}$$

The occurrence of HVSs is inferred by very-high values of P_{CWT} (Fig. 5c) compared to that of non-spindling LFPs. Thus, the LFP segment is classified as HVS if P_{CWT} exceeds a predefined threshold.

Performance Metrics

The performance of the online-learning and CWT algorithms is evaluated with reference to the ground-truth in the labeled testing dataset (Section Labeling HVSs by Hilbert-Huang Transform). As the testing dataset exhibits imbalanced number of HVS and non-HVS segments, the detection performance is quantified by the three metrics in Eqs. (5)–(7) where true positive (TP) refers to correct detection of HVS. Misclassification of a HVS or a non-HVS is denoted as a false negative (FN) or a false positive (FP), respectively.

The *recall* (or *sensitivity*) represents the TP rate, while the *precision* quantifies the ability to detect HVSs correctly. The *F-score* is often used as an overall performance index for the given detection threshold. Based on the performance metrics and detection latency, the optimal TRs are identified for each LFP recording in the training dataset (Supplementary S7).

$$\text{Recall} = \frac{\text{TP}}{\text{TP} + \text{FN}} \tag{5}$$

$$\text{Precision} = \frac{\text{TP}}{\text{TP} + \text{FP}} \tag{6}$$

$$F\text{ - score} = \frac{2 \times \text{Recall} \times \text{Precision}}{\text{Recall} + \text{Precision}} \tag{7}$$

Finally, the performances of the two algorithms with optimal TRs are evaluated in terms of detecting the onset of HVSs in the testing dataset.

RESULTS

The Online-Learning AR_τ Model

Figure 4a shows the exemplar results of learning non-spindling ($< t_{ON}$) and spindling ($\geq t_{ON}$) LFPs by the proposed algorithm, where the onset of HVS (t_{ON}) is determined according to Section Labeling HVSs by Hilbert-Huang Transform. The 144-ms-long, black segment (t_0–t_1 in Fig. 4a) indicates the initial input to the AR_τ model. The model coefficients are then updated according to the error between the predicted LFPs (the dashed blue signal) and the real LFPs (red signal) every 1 ms. Updating both AR_τ coefficients and noises online enables the AR_τ model to accurately predict the spike-and-wave HVSs. As shown in Fig. 4b, the HVS power (P_{AKF} in Section The On-Line Learning Algorithm) estimated at (t_1 + 1) ms is only 0.05, while it is already 0.11 at t_2. P_{AKF} further increases to 1.85 at t_3 owing to the increase in HVS amplitude. With the predetermined threshold (TR = 0.1, Supplementary S7), the HVS is detected with the latency of 36 ms (Fig. 4a), and the detection response for an one-minute-long LFP recording is shown in Fig. 4c. All HVSs are detected with 100% precision and mean latency of 46 ms.

Performance Comparison

Figure 5 compares the performance of the proposed algorithm and CWT in terms of detecting HVSs in the LFPs with different SNRs (8 dB (Fig. 5a), 3.4 dB (Fig. 5e)), where t_{ON} indicates the onset of HVSs. As discussed in Section Performance Metrics, the optimal TRs of the two algorithms are determined from the training dataset (Supplementary S7). The online-learning algorithm (TR = 0.3) detects the HVS 161 ms earlier than the CWT (TR = 0.85μ) in Figs. 5a–5d. The LFPs in Fig. 5e exhibit more spurious oscillations (t_3–t_{ON}), which are suspected to be sleeping spindles.[17] Although these oscillations exhibit highest energy within 3–5 Hz (t_3–t_{ON} in Fig. 5f), the energies in 5-13 Hz are also relatively higher in the period encircled by the dashed-line, as compared with the non-spindling LFPs in Fig. 5b. As a result, the HVS power estimated by the CWT (TR = 0.6 μm) is very sensitive to the spurious oscillations, resulting in three false positives (Fig. 5h). In contrast, the HVS power estimated by the proposed algorithm remains below TR (0.35) during t_3–t_{ON}, while increasing to a large value after t_{ON} in Fig. 5g. Therefore, the proposed algorithm achieves 100% precision (Fig. 5g) and detects the HVS 27 ms earlier than the CWT. These exemplar results indicate that the online-learning algorithm is able to detect the early-onset of HVSs among spurious oscillations, even if these oscillations exhibit similar spectro-temporal features to HVSs. In addition, the time taken by the proposed algorithm and CWT for processing the one-minute- long LFP recording in our computer simulation (with Intel i7 CPU) is 20 and 26 s, respectively.

The performance of the proposed algorithm and CWT is compared more thoroughly over all LFPs in the testing dataset. For the total 1131 HVSs in the testing dataset, the proposed algorithm and CWT achieve mean detection latency of 61 and 74 ms,

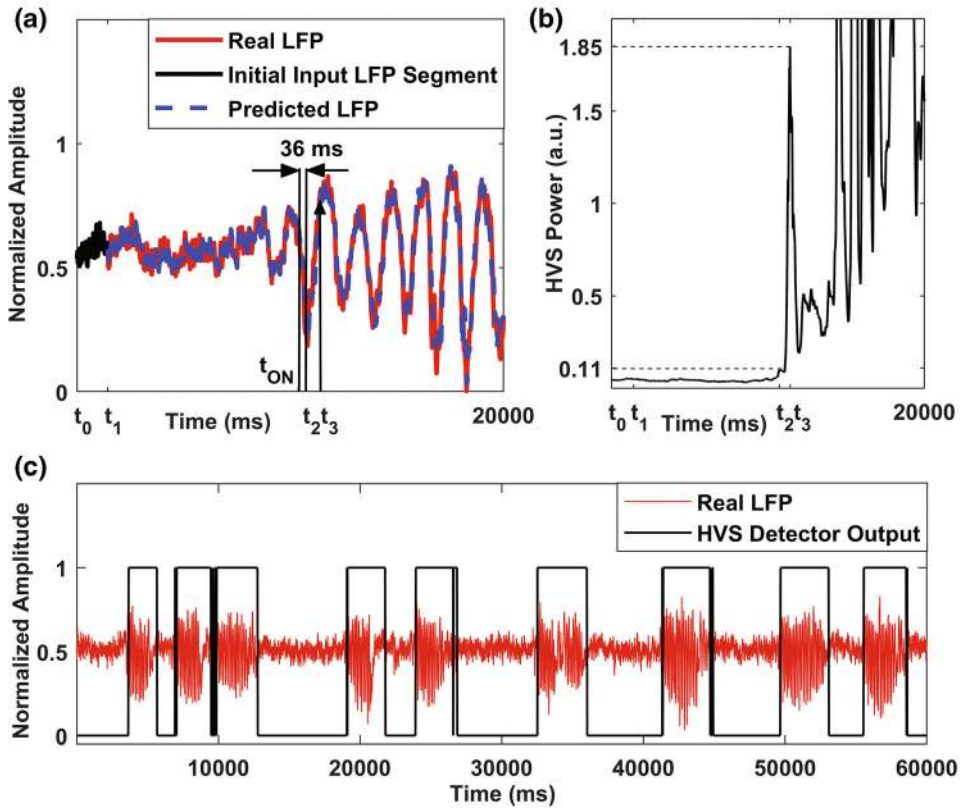

FIGURE 4. (a) Prediction by the online-learning AR_c model for the LFPs recorded from the primary motor cortex (layer 5b) of R_2. t_0 = 18001 ms, t_1 = 18144 ms, t_{ON} = 19037 ms, t_2 = 19073 ms, t_3 = 19142 ms; (b) Estimated HVS power; (c) Detection response for an one-minute-long LFP recording.

respectively (Table 2). There is a trade-off between detection precision and latency. As short detection latency is more crucial for suppressing the HVSs by cDBS, the optimal TRs are identified for each LFP recording in the training dataset (Supplementary S7). Both methods achieve a perfect recall value of 1, indicating all HVSs are detected. The CWT method achieves lower precision (< 0.8) for the 6th LFP recording in Table 2. The corresponding LFP recording exhibited relatively more background noise. In contrast, the proposed algorithm achieves not only shorter latency but also better precision and F-score. The improved performance is mainly attributed to online adaptation of both model coefficients and the uncertainty in the AKF. Compared to conventional methods,[6,8,19,22,24,26] the proposed algorithm requires a prior LFP of only 144 ms (6 samples), much shorter than those required for detecting beta-band synchrony (400 ms in Little *et al.*[19] 1 s in Quinn *et al.*[24] and Rosa *et al.*,[26] and 2 s in Camara *et al.*[6]), or those for detecting HVSs (500 ms in Perumal and Chen[22] and Chen *et al.*[8]). Therefore, the proposed algorithm is computationally-efficient and inherently able to detect HVSs with shorter latency.

DISCUSSION

Motivation Towards Predictive Modeling Approach

The CWT has been shown to detect HVSs using our custom-designed complex Morlet wavelet in Perumal and Chen.[22] The detection latency could be further reduced by decreasing d_L (the separation between successive screening windows). However, the CWT (w_L = 512 ms, d_L = 1 ms) takes 600 s to scan the one-minute-long LFP recording in our computer simulation (Intel i7 CPU). With d_L = 1 ms, the mean latency is reduced only by 10 ms, as compared to the CWT with d_L = 24 ms, for the first LFP recording in Table 2.

These results show that the improved latency achieved by shortening d_L is overshadowed by its huge computational complexity. CWT with d_L = 1 ms requires nearly 23 times longer computing time than CWT with d_L = 24 ms. Therefore, the CWT algorithm (w_L = 512 ms, d_L = 24 ms) is used in this study for performance comparison. Although CWT achieved reliable detection performance (Table 2) across the testing dataset, it is not hardware-friendly for realization in resource-constrained systems. This motivates us

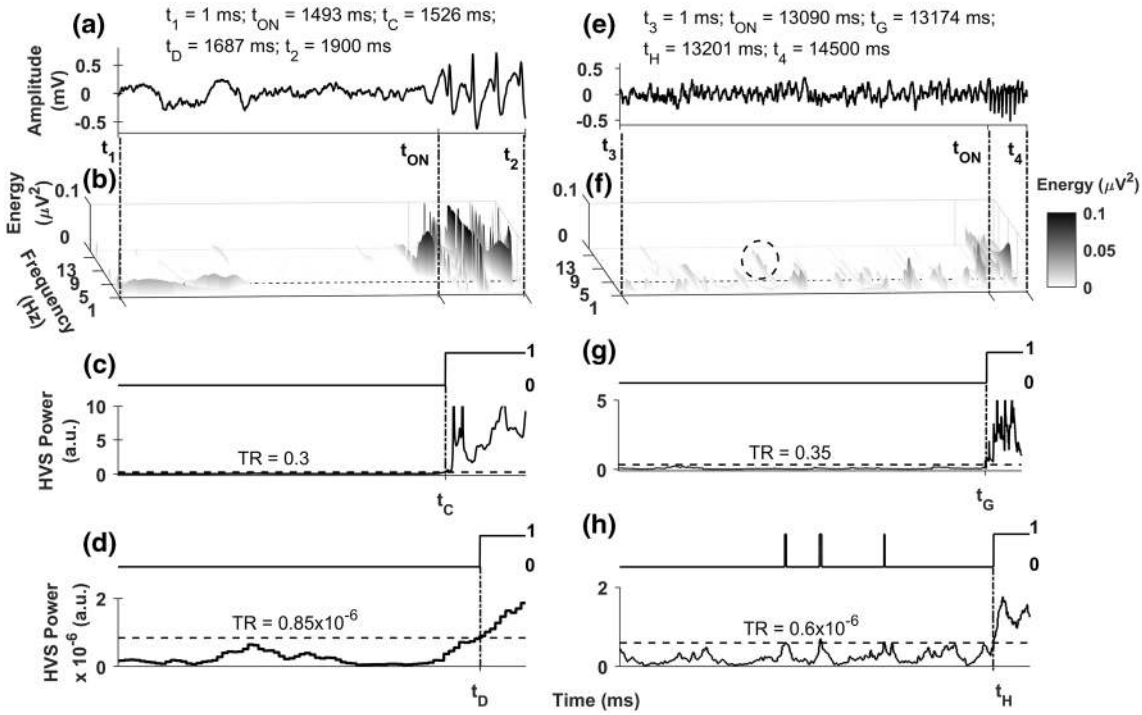

FIGURE 5. LFPs recorded from the (a) primary somatosensory cortex (layer 5b) of R_3, and (e) primary somatosensory cortex (layer 2/3) of R_1 showing spurious oscillations before the onset of HVS (t_{ON}); (b, f) Corresponding time-frequency distributions computed by HHT. Colors are scaled from minimum (white) to maximum (black) values of energy. HVSs exhibit very-higher energy in the 5-13 Hz band during t_{ON}–t_2 (b) or t_{ON}–t_4 (f); Detection response and estimated HVS power showing the early-detection of HVS by the (c, g) online-learning algorithm at t_C and t_G, and (d, h) CWT at t_D and t_H.

to design the computationally-efficient adaptive learning algorithm for a predictive model to detect the early-onset of HVSs.

Advantages of the Online-Learning Algorithm

The proposed algorithm is computationally more efficient, and achieves improved precision (96%) and latency (61 ms) for LFPs recorded from different brain regions of R_1-R_4. The CWT method achieves mean precision of 94% and mean latency of 74 ms, while it requires longer window size (512 samples) and 30% more computation time. Both methods reliably detect the HVSs with sensitivity of 100%. Nevertheless, the AKF tuned both process and measurement noises simultaneously, so that the AR_τ coefficients were updated in accordance with the uncertainty estimated at every time step, as well as the knowledge gained from previous LFP segments. These features enable the proposed algorithm to achieve lower latency and ultimate precision in Table 2.

The proposed algorithm has the following merits. (1) It requires a much shorter prior window (144 ms) of LFPs than the CWT (512 ms). (2) The low dimensionality of AR_τ model ($p^* = 6$) facilitates the detection response from only six samples (out of 144 samples), whereas the CWT uses the entire window of 512 samples. (3) It achieves better precision across the LFPs with spurious oscillations (6th LFP recording in Table 2) than the CWT. (4) Its computation time (20 s) is relatively lower than the CWT (26 s). Furthermore, the Kalman filter has lower computational complexity of $O(3p^{*2})$ for each time step, and has been used for real-time estimation of physiological tremor.[29] Thus, the proposed algorithm is more computationally-efficient and hardware-friendly.

Applicability to Closed-Loop DBS Systems

The proposed algorithm is not only able to detect HVSs but also applicable as a frequency-selective classifier for neuromodulation. For example, synchronous oscillatory beta- and gamma-band activities are found related to schizophrenia.[30] In addition, the loss of nucleus basalis of Meynert neurons resulted in increased HVS episodes (6-10 Hz) associated with spatial memory deficits.[25] For different biomarkers, the AR_τ model parameters can be selected according to the same methods described in Section Materials and Methods, so as to capture distinct target oscillatory features. Automatic detection of different pathological

TABLE 2. Performance comparison between the CWT and online-learning (emboldened) algorithms on the testing dataset.

LFP recording	Brain region*	Rat	HVS bursts	TP	FN	FP	Recall	Precision	*F*-score	Latency (ms)
1	M1D	R_1	70	70	0	8	1	0.9	0.95	106.7
				70	**0**	**2**	**1**	**0.97**	**0.99**	**66.5**
2	M1U	R_1	75	75	0	6	1	0.93	0.96	122.4
				75	**0**	**2**	**1**	**0.97**	**0.99**	**83**
3	M2D	R_1	76	76	0	6	1	0.93	0.96	40.5
				76	**0**	**6**	**1**	**0.93**	**0.96**	**45.5**
4	M2U	R_1	84	84	0	2	1	0.98	0.99	126.3
				84	**0**	**5**	**1**	**0.94**	**0.97**	**55.3**
5	SD	R_1	82	82	0	15	1	0.85	0.92	64.3
				82	**0**	**6**	**1**	**0.93**	**0.96**	**81.9**
6	SU	R_1	85	85	0	36	1	0.7	0.83	113.2
				85	**0**	**13**	**1**	**0.87**	**0.93**	**88.9**
7	STRI	R_1	80	80	0	7	1	0.92	0.96	88.8
				80	**0**	**8**	**1**	**0.91**	**0.95**	**40.2**
8	THAL	R_1	82	82	0	6	1	0.93	0.96	120.1
				82	**0**	**6**	**1**	**0.93**	**0.96**	**77**
9	M1D	R_2	100	100	0	9	1	0.92	0.96	10.6
				100	**0**	**4**	**1**	**0.96**	**0.98**	**45.6**
10	M1U	R_2	110	110	0	9	1	0.92	0.96	106
				110	**0**	**12**	**1**	**0.9**	**0.95**	**54.9**
11	STRI	R_2	4	4	0	0	1	1	1	137.3
				4	**0**	**0**	**1**	**1**	**1**	**37.8**
12	SD	R_2	129	129	0	5	1	0.96	0.98	15.1
				129	**0**	**12**	**1**	**0.91**	**0.96**	**50.4**
13	M1D	R_3	24	24	0	3	1	0.89	0.94	31.6
				24	**0**	**1**	**1**	**0.96**	**0.98**	**76.1**
14	M1U	R_3	25	25	0	2	1	0.93	0.96	58.6
				25	**0**	**1**	**1**	**0.96**	**0.98**	**89.4**
15	STRI	R_3	39	39	0	9	1	0.81	0.9	99.9
				39	**0**	**2**	**1**	**0.95**	**0.98**	**53.3**
16	SD	R_3	23	23	0	0	1	1	1	111.3
				23	**0**	**1**	**1**	**0.96**	**0.98**	**80.7**
17	M1D	R_4	10	10	0	0	1	1	1	17.4
				10	**0**	**0**	**1**	**1**	**1**	**62.1**
18	M1U	R_4	13	13	0	0	1	1	1	21.1
				13	**0**	**0**	**1**	**1**	**1**	**86.5**
19	SD	R_4	10	10	0	0	1	1	1	65.7
				10	**0**	**0**	**1**	**1**	**1**	**31.3**
20	SU	R_4	10	10	0	0	1	1	1	116.8
				10	**0**	**1**	**1**	**0.91**	**0.95**	**33.2**
	Total HVS Bursts		1131	Mean Performance			1	0.94	0.97	73.9
							1	**0.96**	**0.98**	**60.7**

*Brain region: (1) M1D: Layer 5b of primary motor cortex; (2) M1U: Layer 2/3 of primary motor cortex; (3) M2D: Layer 5b of secondary motor cortex; (4) M2U: Layer 2/3 of secondary motor cortex; (5) SD: Layer 5b of primary somatosensory cortex; (6) SU: Layer 2/3 of primary somatosensory cortex; (7) STRI: Dorsal striatum; (8) THAL: Ventrolateral thalamus.

signatures would then improve the DBS treatment for other neurological or psychiatric disorders.

The proposed online-learning algorithm will be realized in FPGA to facilitate real-time, parallel computation in animal experiments. On the other hand, it is interesting to derive a multivariate AR_τ model to learn multi-channel LFPs simultaneously. The learnt coefficients of the multivariate AR_τ model would help to indicate the correlation among different brain regions, revealing how pathological signals are generated and propagated. This understanding would help us to develop novel stimulation protocol for regulating the neural networks efficiently.

ACKNOWLEDGMENTS

The authors gratefully acknowledge the support from the National Health Research Institute [Grant No. NHRI-EX105-10430NI] and the Ministry of Science and Technology [Grant No. MOST 106-2622-8-007-014 -TA] in Taiwan.

REFERENCES

[1]Beudel, M., and P. Brown. Adaptive deep brain stimulation in Parkinson's disease. *Parkinsonism Relat. Disord.* 22:S123–S126, 2016.

[2]Bowerman, B. L., and R. T. O'Connell. Forecasting and Time Series: An Applied Approach. Belmont, CA: Duxbury Press, 1993.

[3]Broersen, P. M. T., and S. de Waele. Time series analysis in a frequency subband. *IEEE Trans. Instrum. Meas.* 52(4):1054–1060, 2003.

[4]Buonamici, M., R. Maj, F. Pagani, A. C. Rossi, and N. Khazan. Tremor at rest episodes in unilaterally 6-OHDA-induced substantia-nigra lesioned rats: EEG-EMG and behavior. *Neuropharmacology* 25(3):323–325, 1986.

[5]Buzsaki, G., A. Smith, S. Berger, L. J. Fisher, and F. H. Gage. Petit mal epilepsy and Parkinsonian tremor: hypothesis of a common pacemaker. *Neuroscience* 36(1):1–14, 1990.

[6]Camara, C., P. Isasi, K. Warwick, V. Ruiz, T. Aziz, J. Stein, and E. Bakstein. Resting tremor classification and detection in Parkinson's disease patients. *Biomed. Signal Process. Control* 16:88–97, 2015.

[7]Carron, R., A. Chaillet, A. Filipchuk, W. Pasillas-Lépine, and C. Hammond. Closing the loop of deep brain stimulation. *Front. Syst. Neurosci.* 7(112):1–18, 2013.

[8]Chen, Y. C., C. C. Chang, R. Perumal, S. R. Yeh, Y. C. Chang, and H. Chen. Optimization and implementation of wavelet-based algorithms for detecting high-voltage spindles in neuron signals. *ACM Trans. Embed. Comput. Syst.* 18(5):1–16, 2019.

[9]Chen, Y. C., R. Perumal, C. H. Hwang, and H. Chen. Hardware-based simplified discrete wavelet transform for detecting high-voltage spindles in neuron signals. 2017 IEEE International Instrumentation and Measurement Technology Conference (I2MTC). Turin, Italy, 2017.

[10]Daniely. A., N. Linial, and S. Shalev-Shwartz. From average case complexity to improper learning complexity. In: Proceedings of the 46th Annual ACM Symposium on Theory of Computing, New York, USA, pp. 441–448, 2014.

[11]De Waele, S., and P. M. T. Broersen. Multirate autoregressive modeling. In: Selected Topics in Signals, Systems and Control, edited by O. H. Bosgra, P. M. J. Van Den Hof, and C. W. Scherer. Amsterdam: IOS Press, 2001, pp. 75–80.

[12]Dejean, C., C. E. Gross, B. Bioulac, and T. Boraud. Dynamic changes in the cortex-basal ganglia network after dopamine depletion in the rat. *J. Neurophysiol.* 100:385–396, 2008.

[13]Ge, S., C. Yang, M. Li, J. Li, X. Chang, J. Fu, L. Chen, C. Chang, X. Wang, J. Zhu, and G. Gao. Dopamine depletion increases the power and coherence of high-voltage spindles in the globus pallidus and motor cortex of freely moving rats. *Brain Res.* 1465:66–79, 2012.

[14]Gilmour, T. P., and T. Subramanian. Multiscale autoregressive identification of neuro-electrophysiological systems. 33rd Annual International Conference of the IEEE EMBS. Boston, USA, 2011.

[15]Hebb, A. O., J. J. Zhang, M. H. Mahoor, C. Tsiokos, C. Matlack, H. J. Chizeck, and N. Pouratian. Creating the feedback loop: closed-loop neurostimulation. *Neurosurg. Clin. N. Am.* 25(1):187–204, 2014.

[16]Huberdeau, D., H. Walker, H. Huang, E. Montgomery, and S. V. Sarma. Analysis of local field potential signals: a systems approach. 33rd Annual International Conference of the IEEE EMBS. Boston, USA, 2011.

[17]Lazic, K., J. Ciric, and J. Saponjic. Sleep spindle dynamics during NREM and REM sleep following distinct general anaesthesia in control rats and in a rat model of Parkinson's disease cholinopathy. *J. Sleep Res.* 28(1):e12758, 2019.

[18]Li, H., S. Kwong, L. Yang, D. Huang, and D. Xiao. Hilbert-Huang transform for analysis of heart rate variability in cardiac health. *IEEE/ACM Trans. Comput. Biol. Bioinform.* 8(6):1557–1567, 2011.

[19]Little, S., A. Pogosyan, S. Neal, B. Zavala, L. Zrinzo, M. Hariz, T. Foltynie, P. Limousin, K. Ashkan, J. FitzGerald, A. L. Green, T. Z. Aziz, and P. Brown. Adaptive deep brain stimulation in advanced Parkinson disease. *Ann. Neurol.* 74(3):449–457, 2013.

[20]Nguyen, D. P., M. A. Wilson, E. N. Brown, and R. Barbieri. Measuring instantaneous frequency of local field potential oscillations using the Kalman smoother. *J. Neurosci. Methods* 184(2):365–374, 2009.

[21]Parastarfeizabadi, M., and A. Z. Kouzani. Advances in closed-loop deep brain stimulation devices. *J. Neuroeng. Rehabil.* 14(1), 2017.

[22]Perumal, R., and H. Chen. Performance analysis in a wavelet-based algorithm for automatic detection of high-voltage spindles in Parkinson's disease rat models. In:

IFMBE Proceedings. 1st Global Conference on Biomedical Engineering & 9th Asian-Pacific Conference on Medical and Biological Engineering, Cham:Springer, pp. 170–173, 2015.
[23]Priori, A., G. Foffani, L. Rossi, and S. Marceglia. Adaptive deep brain stimulation (aDBS) controlled by local field potential oscillations. *Exp. Neurol.* 245:77–86, 2013.
[24]Quinn, E. J., Z. Blumenfeld, A. Velisar, M. M. Koop, L. A. Shreve, M. H. Trager, B. C. Hill, C. Kilbane, J. M. Henderson, and H. Bronte-Stewart. Beta oscillations in freely moving Parkinson's subjects are attenuated during deep brain stimulation. *Mov. Disord.* 30(13):1750–1758, 2015.
[25]Radek, R. J., P. Curzon, and M. W. Decker. Characterization of high voltage spindles and spatial memory in young, mature and aged rats. *Brain Res. Bull.* 33(2):183–188, 1994.
[26]Rosa, M., M. Arlotti, G. Ardolino, F. Cogiamanian, S. Marceglia, A. D. Fonzo, F. Cortese, P. M. Rampini, and A. Priori. Adaptive deep brain stimulation in a freely moving Parkinsonian patient. *Mov. Disord.* 30(7):1003–1005, 2015.
[27]Ross, S. E., Z. Ouyang, S. Rajagopalan, and T. M. Bruns. Evaluation of decoding algorithms for estimating bladder pressure from dorsal root ganglia neural recordings. *Ann. Biomed. Eng.* 46(2):233–246, 2018.
[28]Schlögl, A. The Electroencephalogram and the Adaptive Autoregressive Model: Theory and Applications. Aachen: Shaker-Verlag, 2000.
[29]Tatinati, S., K. C. Veluvolu, S. Hong, W. T. Latt, and W. T. Ang. Physiological tremor estimation with autoregressive (AR) model and Kalman filter for robotics applications. *IEEE Sensors J.* 13(12):4977–4985, 2013.
[30]Uhlhaas, P. J., and W. Singer. Abnormal neural oscillations and synchrony in schizophrenia. *Nat. Rev. Neurosci.* 11(2):100–113, 2010.
[31]Yang, C., J. R. Zhang, L. Chen, S. N. Ge, J. L. Wang, Z. Q. Yan, D. Jia, J. L. Zhu, and G. D. Gao. High frequency stimulation of the STN restored the abnormal high-voltage spindles in the cortex and the globus pallidus of 6-OHDA lesioned rats. *Neurosci. Lett.* 595:122–127, 2015.